Article (refereed) – Published version

Sinha, Bablu; Topliss, Brenda; Blaker, Adam Tobias; Hirschi, Joel Jean-Marie. 2013 A numerical model study of the effects of interannual timescale wave propagation on the predictability of the Atlantic meridional overturning circulation. *Journal of Geophysical Research: Oceans*, 118 (1). 131-146. [10.1029/2012JC008334](#)

A numerical model study of the effects of interannual time scale wave propagation on the predictability of the Atlantic meridional overturning circulation

B. Sinha,[1] B. Topliss,[2] A. T. Blaker,[1] and J.-M. Hirschi[1]

[1]   We investigate processes leading to uncertainty in forecasts of the Atlantic meridional overturning circulation (AMOC). A climate model is used to supply initial conditions for ensemble simulations in which members initially have identical ocean states but perturbed atmosphere states. Baroclinic transports diverge on interannual time scales even though the ocean is not eddy-permitting. Interannual fluctuations of the model AMOC in the subtropical gyre are caused by westward propagating Rossby waves. Divergence of the predicted AMOC with time occurs because the waves develop different phases in different ensemble members predominantly due to differences in eastern boundary windstress curl. These windstress fluctuations communicate with interior ocean transports via modifications to the vertical velocity and the vortex stretching term dw/dz. Consequently, errors propagate westward resulting in longer predictability times in the interior ocean compared with the eastern boundary. Another source of divergence is transport anomalies propagating along the Gulf Stream (and other boundary currents). The propagation mechanism seems to be predominantly advection by mean currents, and we show that the arrival of westward propagating waves can trigger development of these anomalies. The mean state of the AMOC has a small effect on interannual predictability in the subtropical gyre, most likely because eastern boundary windstress curl predictability is not strongly dependent on the state of the AMOC in the subtropics. Eastern boundary windstress curl was more predictable at 45°N when the AMOC was in a strongly decreasing state, but, unlike at 30°N, no mechanism was found linking windstress curl fluctuations with deep transports.

1.   Introduction

[2]   Variability and predictability of the Atlantic meridional overturning circulation (AMOC) and the related topic of decadal predictability of climate have been subjects of scientific interest since the first global coupled ocean-atmosphere models were constructed [e.g., *Manabe and Stouffer*, 1988]. In the majority of cases, the preferred index of the thermohaline circulation has been the maximum of the overturning stream function, which for simulations of present-day climate with ~1° horizontal resolution in the ocean is usually found at ~45°N and ~1000 m depth. More recent higher resolution ocean models tend to differ, e.g., in ¼° and 1/12° simulations of the NEMO ocean model, the maximum AMOC occurs at about 30°N–35°N [*Hirschi et al.*, 2012]. The earliest studies, working with flux-corrected models found substantial variability of the AMOC on interannual to decadal time scales and sought to explain this variability. For example *Delworth et al.* [1993] found that AMOC fluctuations in the GFDL climate model were a result of interplay between gyre and overturning circulations, with temperature fluctuations controlling the strength of the gyre which in turn controlled the introduction of salinity anomalies to the sinking region, resulting in a stronger or weaker AMOC which then fed back negatively on the temperature anomalies controlling horizontal gyre strength. A follow up study indicated that for their model, the AMOC fluctuations, while intrinsic to the ocean model, were forced by low frequency fluctuations in atmospheric (heat) fluxes. The same model was also the subject of a perfect model predictability study [*Griffies and Bryan*, 1997], the first in a series of such studies in which ensembles of simulations are run with identical initial ocean states and slightly perturbed atmosphere states. Subsequent divergence in climate variables between ensemble members then gives an indication of the potential predictability of those

[1]National Oceanography Centre, European Way, Southampton, Hampshire, UK.

[2]Fisheries and Oceans, BIO, Canada.

Corresponding author: B. Sinha, National Oceanography Centre, European Way, Southampton SO14 3ZH, Hampshire, UK. (bs@noc.ac.uk)

variables (given imperfect knowledge of the initial conditions, but a perfect model). Following these pioneering studies many more coupled ocean atmosphere models have been developed with higher resolution and more sophisticated parameterizations of physical processes. In particular the HadCM3 model [*Gordon et al.*, 2000] has been the subject of extensive analysis and displays AMOC variability at a number of timescales: decadal [*Dong and Sutton*, 2005], centennial [*Vellinga and Wu*, 2004], and millennial [*Hawkins and Sutton*, 2007]. The HadCM3 model is also used operationally to provide decadal forecasts of global temperature [*Smith et al.*, 2007], one of a small number of models used routinely for this purpose. Most previous analysis has focused on the maximum of the AMOC as a suitable index of the Atlantic thermohaline circulation and have concentrated on the temperature/salinity/density structure of the model solution and attempted to explain variability in the THC based on analysis of those variables. Moreover predictability studies have so far concentrated on determining the time scale of predictability of various variables and also on finding links between THC predictability and climate predictability [*Collins and Sinha*, 2003]. Here we argue that to understand error growth in predictability studies one must look at the physical mechanisms causing amplification of small initial differences.

[3] On annual time scales a major source of variability in the North Atlantic is thought to be propagation of Rossby waves originating from the eastern boundary where they are hypothesized to be generated by fluctuations in wind stress curl [*Barnier*, 1988], although in principle they can be generated at any location [*Killworth and Blundell*, 2007]. Rossby waves have been described by classical geophysical fluid dynamics theory [e.g., *Gill*, 1982] and have been invoked to explain in situ observations [e.g., *Siedler and Finke*, 1993] fitted a Rossby wave model to mooring data from the Canary Basin) as well as westward propagating features in sea surface height fields derived from satellite altimetry [e.g., *Cipollini et al.*, 1999]. Whilst there is still ongoing debate concerning whether the propagating features are truly Rossby waves rather than propagating eddies [e.g., *Pingree and Sinha*, 2001; *Chelton et al.*, 2007], and what factors determine the observed phase speed, there is a consensus that westward propagation is real, a conclusion bolstered by the wealth of model simulations predicting westward propagation [e.g., *Barnier*, 1988; *Hirschi et al.*, 2007; *Lecointre et al.*, 2008]. The source of westward propagation is another issue. Windstress curl at the eastern boundary has been suggested as the source in both numerical model studies [*Lippert and Kase*, 1985; *Gerdes and Wübber*, 1991] and observations (*Sturges and Hong* [1995], *Polito and Cornillon* [1997], and more recently, *Mason et al.* [2011]). However, to our knowledge, the precise mechanism by which wind forcing at the eastern boundary forces a Rossby wave response has not been investigated in a full primitive equation ocean general circulation model. Additionally, most attention has been focused on annual period waves/propagating features and little to longer periods (interannual and decadal). Measurements made by the RAPID (Rapid Climate Change)/MOCHA (Meridional Overturning Circulation and Heat Transport Array) monitoring array at 26.5°N in the Atlantic [*Kanzow et al.*, 2009] have revealed that the AMOC displays variability on many time scales, ranging from sub monthly to interannual (the ongoing time series is still too short to resolve decadal variability). Variability on

interannual and longer time scales is expected to have a significant impact on climate variability in the North Atlantic region.

[4] In this paper, our investigation of error growth in meridional transport leads us to the conclusion that westward propagating features (with the characteristics of Rossby waves) forced by windstress curl variability at the eastern boundary are a major factor in causing divergent meridional transports in the subtropical and subpolar gyre regions of the North Atlantic on (annual and) interannual time scales. The windstress is found to communicate with the ocean via changes to the near surface vertical velocity and subsequently by changes to the vortex stretching term dw/dz, which causes a response in the meridional transport.

[5] The remainder of this paper is organized as follows: section 2 sets out some theoretical expectations for the physical sources of error growth based on the equations of motion. Section 3 describes the model and analysis methods; section 4 describes the model meridional overturning circulation and investigates its variability and predictability on interannual time scales, showing the importance of westward wave propagation and windstress at the eastern boundary, and potential dependence on the mean strength of the AMOC. We present a summary and discussion of our results in sections 5 and 6.

2. Theoretical Considerations

[6] In a first step we look at the basic force balances found in the equations governing the ocean circulation with the aim to highlight the terms which are most likely to cause diverging model trajectories.

2.1. Relationship Between Transport and Pressure Gradient

[7] We take the geostrophic balance as our starting point. In standard notation

$$fv = \frac{1}{\rho_0} \frac{\partial P}{\partial x}, \qquad (1)$$

$$fu = -\frac{1}{\rho_0} \frac{\partial P}{\partial y}, \qquad (2)$$

where x and y are eastward and northward coordinates (in a local Cartesian frame of reference), u and v are the corresponding components of seawater velocity, P is the (hydrostatic) pressure, ρ_0 is a reference density for seawater, and $f = 2\Omega\sin\theta$ is the Coriolis parameter (where Ω is the Earth's rotation rate and θ is the local latitude).

[8] Concentrating on the meridional component of velocity, we define depth (z) averaged (barotropic) and baroclinic components, $\bar{v}$ and v', respectively, for an ocean depth H

$$\bar{v} = \frac{1}{H} \int_{-H}^{0} v \, dz, \qquad (3)$$

$$v' = v - \bar{v}. \qquad (4)$$

[9] The equation for the barotropic component is

$$f\bar{v} = \frac{1}{\rho_0 H} \int_{-H}^{0} \frac{\partial P}{\partial x} \, dz. \qquad (5)$$

[10] As HadCM3 employs the rigid lid approximation, the pressure P can be written in terms of the density field as follows:

$$P = P_{\text{rigidlid}} + \int_z^0 \rho g \, dz. \qquad (6)$$

[11] Hence, we can write

$$f\bar{v} = -\frac{1}{\rho_0} \frac{\partial P_{\text{rigidlid}}}{\partial x} + \frac{1}{\rho_0 H} \int_{-H}^0 \frac{\partial}{\partial x}\left(\int_z^0 \rho g \, dz'\right) dz. \qquad (7)$$

[12] For the baroclinic component we have

$$
\begin{aligned}
-fv' &= -\frac{1}{\rho_0}\frac{\partial P}{\partial x} + \frac{1}{\rho_0 H}\int_{-H}^0 \frac{\partial P}{\partial x}\,dz, \\
&\approx \frac{\partial}{\partial x}\left(-\frac{1}{\rho_0}\int_z^0 \rho g\,dz + \frac{1}{p_0 H}\int_{-H}^0\int_z^0 \rho g\,dz'dz\right),
\end{aligned}
\qquad (8)
$$

where the approximation refers to the fact that the ocean depth is a function of position and hence the depth integral of the pressure gradient is not in general equal to the gradient of the depth integral of the pressure. The advantage of making this approximation is that the geostrophic transport across a given section can be related to the pressure difference between its endpoints. Errors due to this approximation are likely to be largest where there is variable bottom topography across a section. Nonetheless, as the endpoint pressures are measurable in the real world, it is of interest to examine how well this approximation holds in the model. Note that the barotropic flow is difficult to measure and P_{rigidlid} is related to an unknown surface setup, bottom pressure or level of no motion and here we focus largely on the baroclinic pressure gradient. A similar decomposition was performed by *Sime et al.* [2006].

[13] We can obtain a further useful relationship by cross differentiation of equations (1) and (2)

$$\frac{\partial}{\partial y}(fv) + \frac{\partial}{\partial x}(fu) = \frac{1}{\rho_0}\frac{\partial^2 P}{\partial y \partial x} - \frac{1}{\rho_0}\frac{\partial^2 P}{\partial x \partial y} \equiv 0, \qquad (9)$$

which reduces to

$$f\left(\frac{\partial v}{\partial y} + \frac{\partial u}{\partial x}\right) + v\frac{\partial f}{\partial y} = 0, \qquad (10)$$

setting the meridional variation of the Coriolis parameter, df/dy to be β and noting that continuity requires $du/dx + dv/dy + dw/dz = 0$ for a rigid lid model, then

$$\beta v = -f\frac{\partial w}{\partial z}. \qquad (11)$$

[14] That is, neglecting the relative vorticity, vortex stretching must be balanced by north-south movement of a water column to conserve potential vorticity.

[15] We also make use of the well-known expression relating near-surface vertical velocity, w_{Ek}, to local windstress, τ (Ekman pumping)

$$w_{\text{Ek}} = \frac{1}{\rho_0 f} curl_z \tau. \qquad (12)$$

[16] But instead of using the local windstress we will look for relationships between near surface vertical velocity and windstress on the eastern boundary as discussed in section 1.

2.2. Definition of AMOC and AMOC Index

[17] Following many previous authors, we define the AMOC, ψ, as

$$\psi(y,z) = \int_{-H}^z \int_{x_e}^{x_w} v(x,y,z')\,dx\,dz', \qquad (13)$$

where x_w and x_e are the x coordinates of respectively the western and eastern sides of the Atlantic Basin. In common with *Collins and Sinha* [2003] we use the value of the AMOC at 45°N and ~670 m depth as an index of the overall strength of the AMOC, however we also examine AMOC predictability further south at 30°N as this is where extensive observations from the RAPID array [*Cunningham et al.*, 2007] are available.

3. Methods

[18] We analyze data from a 100 year portion (years 561–660) of the 4000+ year HadCM3 preindustrial control simulation [*Gordon et al.*, 2000], hereinafter referred to as "CONTROL") and two sets of 20 year simulations which ran the same model configuration with perturbed atmospheric initial conditions starting from different points of CONTROL. The method of performing additional simulations with slightly perturbed initial atmospheric conditions is described in detail by *Collins and Sinha* [2003] and the data used here is a subset of that used by those authors. Briefly, on 1 December of years 590 and 633, respectively, CONTROL was rerun for a short period (4 days), with the atmospheric state output at the end of each model day. These 4 slightly different atmospheric states were then used to initialize HadCM3 on 1 December of years 590 and 634, along with the original ocean state from CONTROL, resulting in five-member ensembles of HadCM3 simulations (counting CONTROL as one member) with identical ocean initial conditions but perturbed atmospheric initial conditions.

[19] Apart from examination of the traditional AMOC index (equation (13), section 2.2), we diagnose depth integrated baroclinic transports and baroclinic pressure gradients. We perform (lagged) correlation analysis for pairs of variables to elucidate the physical processes controlling transport fluctuations. Average transports are calculated for two depth ranges, 100–650 m and 650–3500 m, hereinafter referred to as the "upper" and "lower" layers respectively. The upper layer is made up of predominantly northward flowing thermocline waters, whilst the lower layer consists of southward flowing North Atlantic Deep Water in the model (section 4).

[20] In year 590 the control AMOC index was in a relatively high state, or more precisely there was a decreasing trend on decadal timescales, whilst in year 633 it was in a relatively low state (increasing trend on decadal timescales),
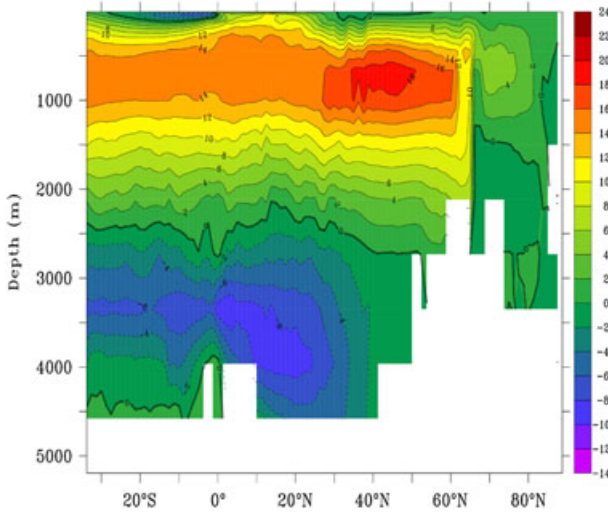
Figure 1. AMOC (Sv) from CONTROL based on monthly mean velocities (100 year average). Positive (negative) values imply clockwise (anticlockwise) circulation.

hence our model study allows us to assess the dependence of predictability of the AMOC on the state of the AMOC. We refer to the two ensembles as "HIGH" and "LOW" respectively. Analysis is performed on seasonal means (December-January-February, March-April-May, June-July-August, and September-October-November) and also on band-pass (retaining periods of 1–4 years inclusive) and low-pass filtered data (retaining periods greater than 4 yrs). The filtering method is described by *Hirschi et al.* [2007]. A mean seasonal cycle based on CONTROL is always subtracted from the signal before filtering is applied.

4. Results

4.1. Simulated Atlantic Meridional Overturning Circulation

[21] The mean AMOC simulated by the HadCM3 control averaged over the 100 year analysis period (from monthly

mean velocity data) is shown in Figure 1. This figure is familiar from many previous studies [*Gordon et al.*, 2000]. It shows a maximum Atlantic overturning of ~19 Sv at about 45°N and ~650 m depth, with northward surface flow (thermocline waters), sinking at about 60°N–65°N, and return flow of Upper North Atlantic Deep Water between depths of 650–2500 m. There is a 5 Sv overturning in the Arctic Ocean with sinking to depths of about 1500 m between 75°N–80°N. The Arctic Bottom Water upwells at around 65°N and exits to the Atlantic basin. There is also an inflow of Antarctic Bottom Water (about 6 Sv) from the Southern Ocean, below about 3500 m. It penetrates as far as about 40°N. Upwelling takes place between 20°N–40°N and the water recirculates as Lower North Atlantic Deep Water. About 25 Sv of water exits the Atlantic between 650—3500 m depth. We can define two levels of no motion for the Atlantic basin consistent with Figure 1: the 650 m level and the 3500 m level. This provides the rationale for our division of the volume transport into two main layers, one between 100–650 m which represents the northward flowing thermocline waters (and excludes the surface (Ekman) layer which is under the direct influence of surface windstress), and one between depths of 650–3500 m which represents the southward flowing North Atlantic Deep Water.

[22] The variability of the AMOC at 45°N and 30°N is shown in Figures 2a and 2b. Variability of similar amplitude on seasonal, interannual, decadal and multidecadal time-scales is apparent to the eye. Over the 100 year period, the AMOC varies between 15 and 23 Sv at 45°N and between 6 and 22 Sv at 30°N. Predictability can be measured as the extent to which members of an ensemble track each other in time (via Anomaly Correlation Coefficient, ACC, *Collins* [2002]) or as the extent to which the spread in the ensemble is comparable to the climatological spread (via root mean square error, RMSE). The initial condition ensembles are also shown in Figures 2a, and 2b and the results indicate that some predictability is present, particularly at decadal time scales [*Collins and Sinha*, 2003]. However annual and interannual variability is large which would give rise to considerable uncertainty if an actual forecast were being made.
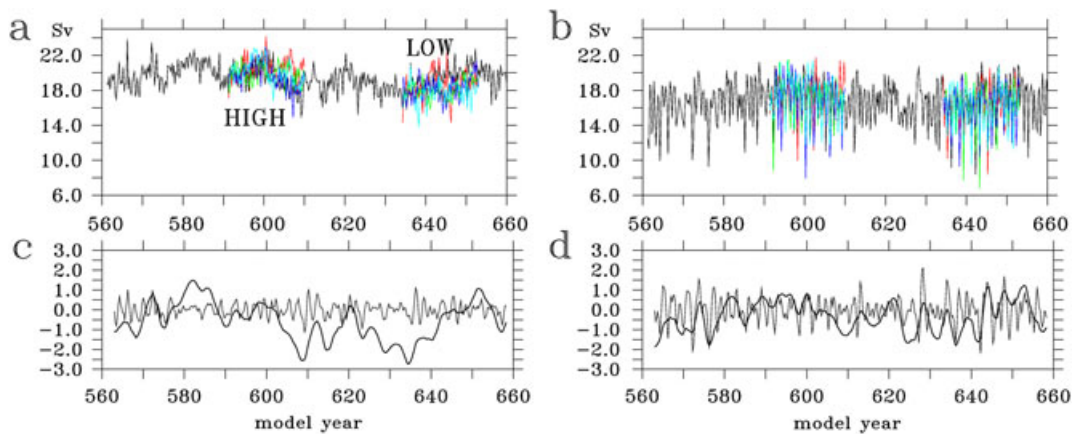

Figure 2. (a) Time series of AMOC (Sv) at ~650 m depth from CONTROL at 45°N based on seasonal mean velocities (black line). Colored lines represent the time series for individual members of ensembles HIGH and LOW (also based on seasonal means). (b) Similar time series at 30°N. (c) AMOC variability at 45°N in CONTROL split between interannual (thin line) and decadal (thick line) time scales. (d) Corresponding time series at 30°N.

Table 1. Standard Deviation at 45° and 30°N of the AMOC (Sv) for Different Time Scales, Calculated From Years 561–660 of CONTROL

	45°N	30°N
Seasonal	0.81	1.87
Interannual	0.36	0.67
Decadal	0.96	0.76
Total	1.44	2.47

Interestingly, compared to CONTROL, there is a tendency for all the ensemble HIGH members to be biased high and the ensemble LOW members to be biased low. This could be related to the way in which the ensemble members are perturbed and to our knowledge has not been noted for ocean models before.

[23] We can split the AMOC index into components corresponding to interannual (1–4 year) time scales and longer (>4 year) time scales respectively using time-domain bandpass and lowpass filters, Figures 2c, and 2d, following the method of *Hirschi et al.* [2007]. Figure 2c makes it clear that at 45°N the variability on interannual time scales has a smaller amplitude compared with that on decadal time scales (~4 Sv peak-to-peak on longer time scales compared with ~2 Sv peak-to-peak on interannual time scales). On the other hand at 30°N the corresponding amplitudes are of similar magnitude (about 3Sv peak-to-peak in both cases). As a further measure of variability, the standard deviation of the AMOC is tabulated for various time scales at 45°N and 30°N (Table 1). At 45°N the decadal variability is more than twice as large as the interannual variability (0.96 Sv compared to 0.36 Sv), whilst at 30°N they are of the same order (0.67 Sv compared to 0.76 Sv). In absolute terms, decadal variability is larger at 45°N (0.96 Sv) than at 30°N (0.76 Sv), and interannual variability is much smaller (0.36 Sv at 45°N and 0.67 Sv at 30°N). It is also noteworthy that the seasonal variability is much stronger at 30°N compared with 45°N (1.87 Sv compared with 0.81 Sv). In comparison with direct observations of the AMOC, HadCM3 displays good agreement at subannual-annual time-scales as reported by *Balan Sarojini et al.*, [2011]. Based on 5-day means, HadCM3 has a mean transport of 17.1 Sv and a standard deviation of 4.1 Sv which compares well with 18.6 and 4.5 Sv respectively derived from the RAPID array. Note

that the RAPID observational AMOC time series is still too short to adequately filter on interannual or longer time scales.

[24] Our focus in this paper is on interannual variability, since variability on this time scale is substantial, is expected to have an influence on North Atlantic climate and is reasonably well resolved by direct measurements of the MOC. Therefore, in what follows we will concentrate mainly on variability and predictability on interannual time scales.

4.2. Relationship Between Transport and Pressure Gradient

[25] As indicated in section 2, our expectation is that the flow will be largely geostrophic in the ocean interior and we thus should be able to explain the divergence in the volume transport (i.e., the AMOC) in terms of changes in the pressure gradient (equation (8)). However it is important to check how accurately the model flow field is consistent with theory in this regard [cf. *Gregory and Tailleux*, 2011]. Therefore, we next examine the relationship between baroclinic transport and baroclinic pressure gradients for surface and lower layers, for interannual time scales (Figure 3). One possible error when performing correlations where there is a large seasonal signal, is aliasing of the seasonal cycle to lower frequencies. We have made extensive checks of time series at individual gridpoints and have found no evidence of contamination of bandpass filtered data with a seasonal signal. Correlations are generally high (0.8–0.9) except at the western and northern boundaries of the Atlantic basin, along the mid-Atlantic Ridge, and close to the equator where correlations drop to values in the range 0.3–0.6. The correlation is not plotted in regions shallower than ~650 m but it generally weakens further (note that smoothing has been applied to remove gridpoint noise in the pressure field, so in Figure 3 the ocean continental shelves appear wider and are eliminated as too shallow). In the lower layer, correlations remain high and even close to the western boundary we find reasonably high correlations of order 0.8 suggesting that a significant portion of the meridional flow is geostrophic and can be related to the pressure gradient across the section (even where there is a significant topographic slope as discussed in section 2). In the South Atlantic a similar situation occurs, but whereas geostrophy is maintained
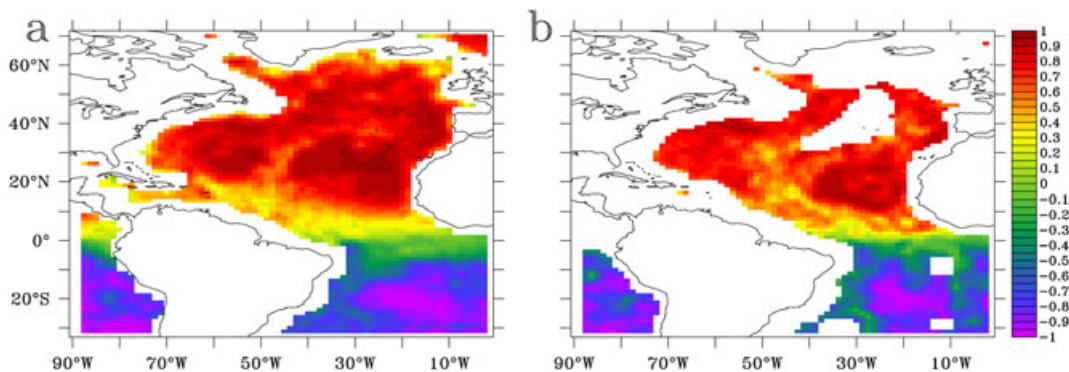

Figure 3. Correlation coefficient between baroclinic transport anomaly (Sv) and baroclinic pressure gradient anomaly (evaluated as a pressure difference with units hPa) for interannual time scales: (a) upper layer and (b) lower layer. The correlation is not evaluated where the depth is too shallow to calculate a pressure gradient for the defined depth ranges. Analysis is performed on monthly mean anomalies with respect to a monthly mean climatology from CONTROL.
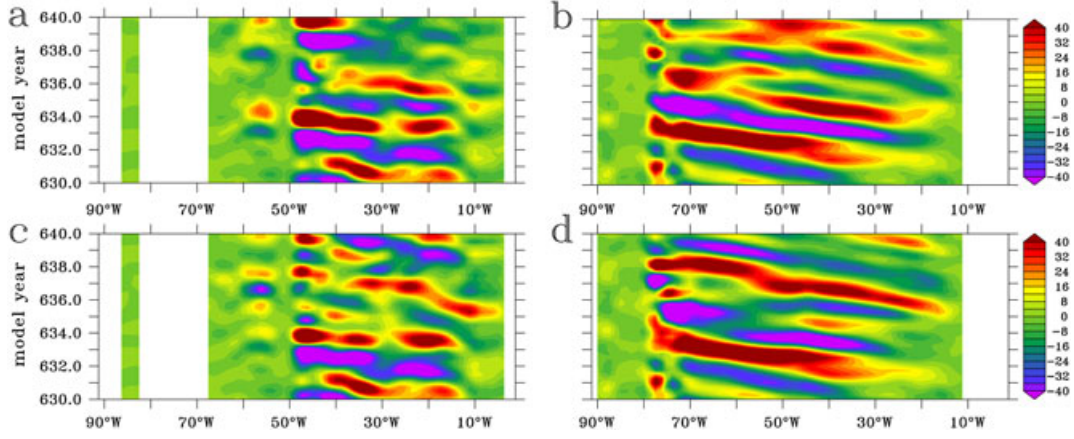
Figure 4. Longitude-time diagrams of upper layer baroclinic pressure anomaly (hPa) with interannual filter for two members of ensemble LOW (a) first member at 45°N, (b) first member at 30°N, (c) fourth member at 45°N, and (d) fourth member at 30°N.

to high accuracy in the deep ocean basins (correlations of order −0.9), the correlations are much weaker close to the coast (weaker than –0.6 in the upper layer and of order –0.4 in the lower layer). Figure 3 is based on a 30 year portion of CONTROL starting 10 years before the period of the HIGH ensemble, but the pattern illustrated is robust across a similar portion overlapping the LOW ensemble period and across the ensemble members. The accuracy of the geostrophic balance is thus similar across two different portions of CONTROL and across the ensemble members.

[26] We conclude that the pressure gradient in general gives a good indication of the transport except at the equator. Therefore we are justified in attributing changes in transports to changes in the pressure/density. Thus to explain transport variability we need to explain variability in the pressure field. The relationship is weaker at the western boundary, particularly at the shallower depths not shown in Figure 3 and we cannot always assume that pressure anomalies will result in transport anomalies at the western boundary.

4.3. Causes of Interannual Variability

[27] The origin of the interannual variability noted in section 4.1 can be found by plotting longitude-time diagrams of upper layer baroclinic pressure anomalies. A typical example is plotted in Figure 4 (in this case for ensemble LOW, but the features are typical across ensembles and ensemble-members), at latitudes 45°N and 30°N. We see alternating bands of positive and negative anomalies. At 45°N (Figure 4a) there is evidence of propagation taking place intermittently, but at 30°N there is clearly continuous propagation of anomalies apparent from the east-west tilt of the isolines (Figure 4b) originating at the eastern boundary and propagating westward, taking ~3–4 years to reach the western boundary, a speed of ~5.3 cm/s at this latitude. There appears to be some amplification at the western boundary and also over the mid-Atlantic ridge. However, in the shallow westernmost region there is a significant decrease in variability. This is consistent with the behavior of other models (e.g., OCCAM, *Hirschi et al.* [2009]) and also with results from the RAPID monitoring array, *Kanzow et al.* [2009].

[28] By examining similar diagrams for a different ensemble member (Figures 4c and 4d), we see that, while the speed of propagation is similar between the two simulations, the amplitude and phase of the propagating features is different which will undoubtedly affect the baroclinic transport through the previously verified geostrophic relation (Figure 3), to a large extent in the mid ocean regions where the geostrophic relation is strongest, but also to a lesser extent at the western boundary (see sections 4.6 and 4.7 for more detailed analysis of the western boundary region).

[29] The propagating features which cross the basin at 30°N are reminiscent of first baroclinic Rossby waves (as previously suggested by *Dong and Sutton* [2002]) and their phase speeds fit with the theoretical wave speed derived from the model stratification climatology. Propagation occurs at these time scales in the control simulation, and also in all the members of the two ensembles, HIGH and LOW.

[30] The depth structure of the anomalies is shown in Figure 5, which plots the baroclinic pressure anomaly as a function of depth and time at a particular location (40°W, 30°N). Surface and deep pressure anomalies are in antiphase, which indicates a mode 1 (i.e., first baroclinic) Rossby wave at this location. The depth structure projects strongly onto the AMOC (enhanced upper layer transport is associated with enhanced lower layer transport) and implies systematic changes to meridional ocean heat transport as the wave propagates.

4.4. Effects of Wave Propagation on Predictability

[31] Having established that all ensemble members (both HIGH and LOW states) show wavelike propagation on interannual time scales, but with different phases (Figure 4), we are now in a position to examine the effects of these waves on the divergence in time of the transports between ensemble members. Figure 6 shows the RMS difference in baroclinic pressure anomaly between ensemble members for the two ensembles LOW and HIGH at 45°N and at 30°N as a function of longitude and time for the upper layer on interannual time scales. As an indication of robustness of our results to ensemble size, we doubled the number of members in ensemble LOW and found no qualitative difference in the RMSE estimates (Figures 6 and 7).

[32] A formal measure of predictability, the RMSE, takes into account all ensemble members. Here the root mean
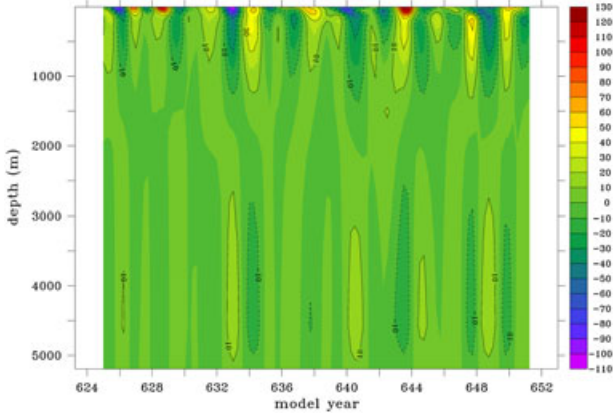
Figure 5. Interannually filtered baroclinic pressure anomaly (hPa) from CONTROL as a function of depth and time at 40°W, 30°N.

square difference in pressure between pairs of ensemble members, normalized by twice the climatological standard deviation from CONTROL (2σ, see *Collins and Sinha* [2003]) is plotted as a function of lead time. As in Figure 4, at 45°N (Figures 6a and 6c) there is evidence of intermittent westward propagation and for the HIGH ensemble, the largest errors set in first close to the eastern boundary (15°W–30°W). There is thus higher predictability in the western basin (by 1–3 years) in this case. For the LOW ensemble (Figure 6c), larger errors set in at about the same time on both boundaries and there is greater predictability in the interior ocean (~30°W). A clearer picture emerges at 30°N (Figures 6b and 6d) where there is continuous westward propagation from the eastern to the

western boundary. In the LOW ensemble particularly (Figure 6d) there is a definite difference in predictability of a few years between eastern and western basins. This is less clear for ensemble HIGH (Figure 6b), but both ensembles show a region of low RMSE growth between about 75°W and 85°W (i.e., on the narrow and shallow shelf region of the western boundary). At both 45°N and 30°N the LOW ensemble appears to have a shorter predictability time close to the eastern boundary (within 5°–10°) compared with the HIGH ensemble. Taken together, Figures 4 and 6 suggest that given some knowledge of what is happening on the eastern boundary, one could predict subsequent variations in many parts of the western basin. The lower layer pressure difference (not shown) shows similar features.

[33] We conclude this section by examining the RMSE of the AMOC itself (i.e., the basin integrated transport) rather than local transports (Figure 7). At both 45°N and 30°N, the RMSE of the AMOC displays the signature of interannual variability. At 45°N (Figure 7a), there is a clear difference between the HIGH and LOW ensembles. In the HIGH ensemble, the RMSE stays at or below the standard deviation of CONTROL (green line) for around 7 years, implying the model has some prediction skill. In the LOW ensemble by contrast the RMSE stays above the CONTROL standard deviation for most of the first decade, implying much less predictability. At 30°N, both HIGH and LOW ensemble RMSEs rise above the level of the CONTROL standard deviation after about a year, consistent with the larger amplitude of interannual fluctuations noted in Figure 2. Without further investigation it is unclear exactly how the RMSE of the AMOC is related to the westward propagation, but the RMSE due to the westward propagation (Figure 6) is the
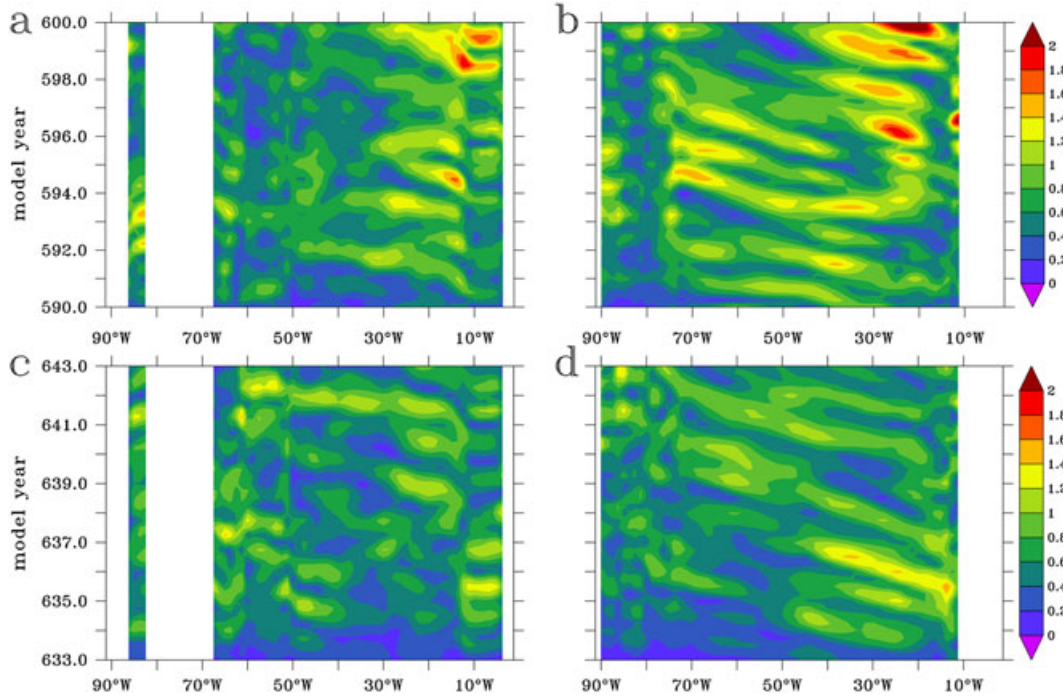

Figure 6. Longitude-time diagram of RMSE (normalized by twice the standard deviation of the CONTROL time series) in upper layer baroclinic pressure anomaly with an interannual filter (a) ensemble HIGH 45°N, (b) ensemble HIGH 30°N, (c) ensemble LOW 45°N, and (d) ensemble LOW 30°N. Note that 10 years of CONTROL data are prepended to each ensemble member before the interannual filter is applied.
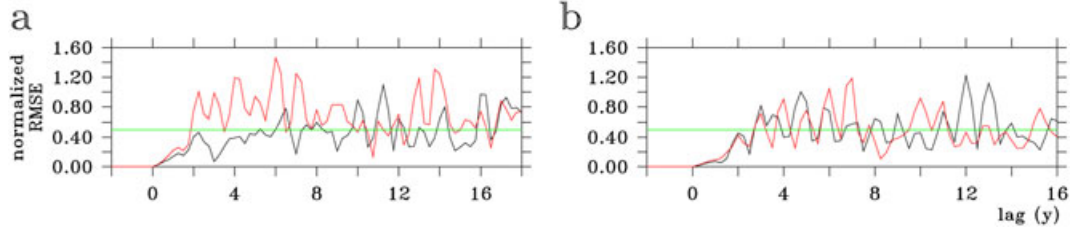
Figure 7. RMSE of the AMOC at (a) 45°N and (b) 30°N for ensemble HIGH (black lines) and LOW (red lines) as a function of lead time (the start time of each ensemble is arbitrarily shifted to year 2 for comparison). The RMSE has been normalized by twice the standard deviation of CONTROL. Calculations are based on interannually filtered seasonal mean data. The green lines show the level at which the RMSE equals the CONTROL standard deviation. RMSE is nonzero before year 2 due to interannual filtering and the prepending of CONTROL data (see Figure 6 caption).

right order of magnitude to explain the signal seen in the RMSE of the AMOC. The reasonable correspondence between the AMOC variability in HadCM3 compared with observations (section 4.1) enables us to tentatively conclude that the Rossby wave mechanism could be of substantial importance in explaining the observed variability. We return to the subject of the link with the basin integrated AMOC at the end of section 4.5.

4.5. Mechanism of Generation of Westward Propagating Signals

[34] The hypothesis here is that windstress curl variations on the eastern boundary generate the Rossby wave response seen in the previous sections and that differences in the evolution of the windstress curl between the different members of a given ensemble result in different phases of Rossby wave propagation, giving rise to differences in the transport over time. The mediation between the windstress curl and the Rossby wave generation is hypothesized to act via perturbations to near-surface vertical velocity. A number of studies have linked windstress curl variations to pycnocline depth and hence indirectly to vertical velocity [*Sturges and Hong* 1995; *Kanzow et al.*, 2010; *Chidichimo et al.*, 2010]. Subsequently we expect that there must be modification of the vortex stretching term to affect the meridional transport. Hence, in this section we examine the correlation between windstress curl at the eastern boundary and the near-surface vertical velocity, the correlation between vertical velocity

and the vortex stretching term, and finally the correlation between the vortex stretching term and meridional transport.

[35] Figures 8a and 8b show the correlation (based on equation (12)) between the vertical velocity field at 100 m depth, w_{100m}, and eastern boundary windstress curl (at 23°W, 59°N and at 10°W, 30°N respectively). The relationships are robust across the control run (both high and low periods) and the ensemble members. In Figure 8a there is a strong patch of negative correlations of magnitudes up to about 0.7 in the central subpolar gyre centered at about 36°W, 45°N and positive values to the northeast of about the same magnitude extending along the shelf break from northern Spain to Denmark Strait. In Figure 8b a clear dipole pattern is seen, with an oval patch of negative correlations up to about 0.65 in magnitude in eastern subtropical gyre centered at about 24°W, 33°N and south of this an elongated region of positive correlations of magnitude up to about 0.85 extending from the Spanish and North African coasts across the Atlantic to the northern coast of South America. The strongest positive correlations are in shallow regions adjacent to the North African coast. In summary at lower latitudes wind stress curl on the eastern boundary creates a strong signal just off the eastern boundary in the region where the propagating features originate in the model whereas at higher latitudes whilst there is a strong signal, Figures 4a and 4c show the propagating signals are intermittent and not always coincident (Figure 4a) with the highest correlation between windstress and w_{100m} shown in Figure 8a.
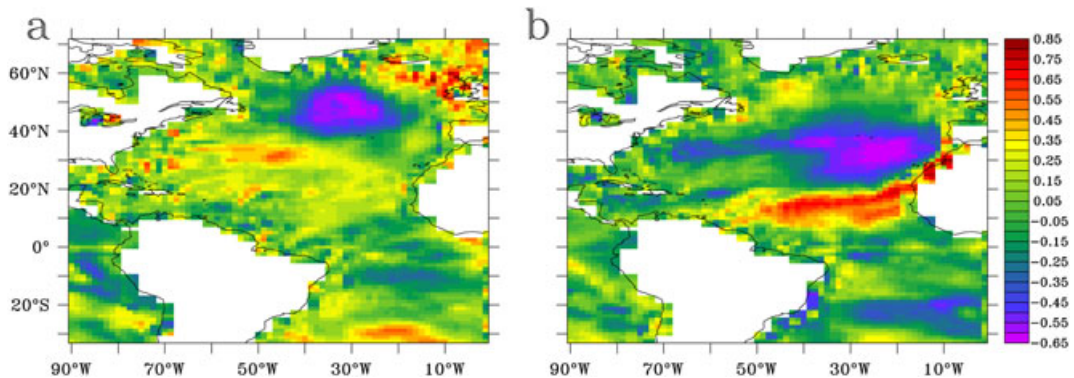

Figure 8. (a) Correlation between windstress curl at the eastern boundary (23°W, 59°N) and vertical velocity at ~100 m depth, w_{100m}. (b) Similar plot for windstress at 10°W, 30°N. Both windstress and vertical velocity have been filtered to retain interannual time scales. Analysis is based on monthly mean anomaly data from CONTROL.
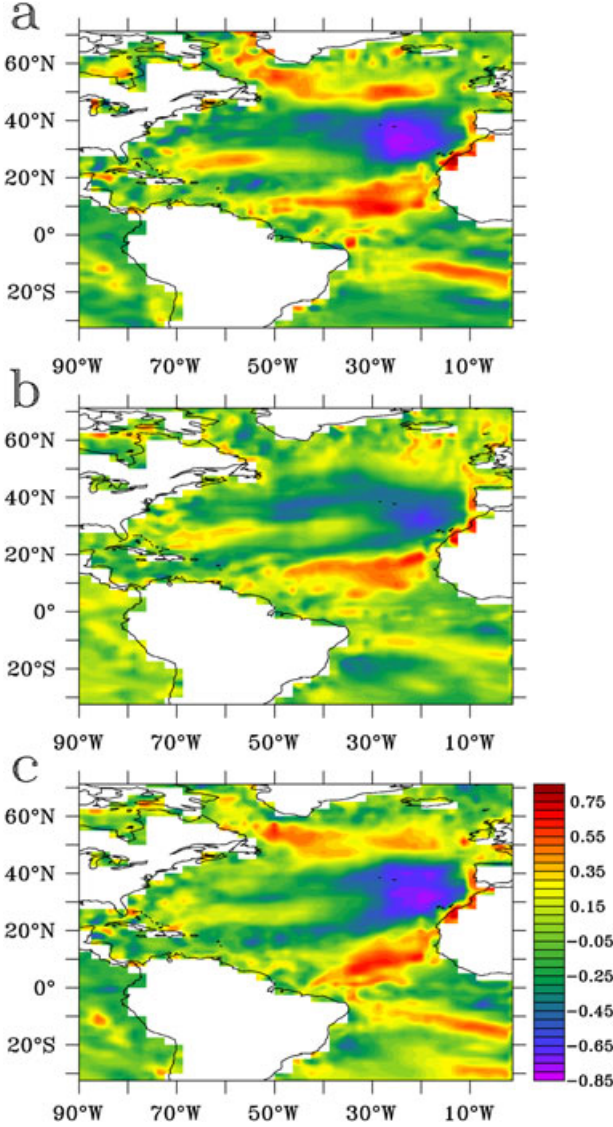
Figure 9. (a) Correlation between windstress curl at the eastern boundary (10°W, 30°N) and vertical velocity at ~100 m depth, w_{100m}, for one of the members of ensemble HIGH. (b) Similar plot for a different member of ensemble HIGH. (c) Similar plot for the correlation between the difference in windstress curl at the eastern boundary, and the difference in near-surface vertical velocity between the two ensemble members. Both windstress and vertical velocity have been filtered to retain interannual time scales. Analysis is based on seasonal mean anomalies with respect to a monthly mean climatology derived from CONTROL.

So at higher latitudes it seems that Rossby waves can be generated and damped across the whole basin and not just at the eastern boundary (see also *Killworth and Blundell* [2003, 2007]) and it is therefore unclear at higher latitudes what role the eastern boundary windstress and associated near surface vertical velocity may play.

[36] As an example of the robustness of the dipole pattern in Figures 8b, 9a, and 9b show similar calculations for two members of ensemble HIGH, that is, the eastern boundary windstress curl at 10°W, 30°N is correlated with the w_{100m}. The patterns reproduce the dipole in Figure 8b, but we note

that the dipole differs in amplitude between the two members. Additionally, the first ensemble member has areas of high correlation not seen in CONTROL or in the other ensemble member. The correlation of the difference in eastern boundary windstress curl at 30°N with the difference in w_{100m} between the two ensemble members is plotted in Figure 9c. The areas of high correlation, positive or negative show that between any two ensemble members the difference in near-surface vertical velocity can be predicted to a large extent by the differences in eastern boundary windstress curl.

[37] We next look for links between w_{100m}, and the vortex stretching term dw/dz, defined for our purposes as the vertical velocity at 100 m minus the vertical velocity at 650 m: $w_{100m}-w_{650m}$ (Figure 10). This time a lagged correlation is required to bring out the relationship. Maximum correlations of about 0.8 occur in a near continuous region extending from Spain to the Western Gulf of Guinea, and penetrating into the central North and South Atlantic subtropical gyres (Figure 10a). There is a progression in phase lag such that $w_{100m}-w_{650m}$ is near instantaneously correlated with w_{100m} near the coastal regions of Spain and North Africa, but lags by up to 15 months in the central subtropical gyre (Figure 10b). It is also noteworthy that correlations are quite low immediately adjacent to the coast of Africa, where w_{100m} is quite strongly correlated with the local windstress curl. A possible explanation of this feature is that the windstress initiates a deeply penetrating wave which hits the sea floor and reflects up again. Some evidence for this can be seen in similar plots to Figure 10a in the vertical plane where the maximum correlations of w_{100m} with meridional transport describe a V shape (not shown). Again the region of strongest correlations is coincident with the generation region of westward propagating waves in the subtropical gyre described in section 4.3. However, there is no clear response in the subpolar gyre, and w_{100m} is disconnected with the vortex stretching there.

[38] We now demonstrate the connection between vortex stretching and meridional transport (equation (11)) to complete our picture of the processes linking boundary windstress curl, and changes in the AMOC. Figure 11 shows the correlation between dw/dz and the northward baroclinic transport integrated over depths of 100–650 m. Large positive correlations are observed in the Northern Atlantic, including subtropical and subpolar gyres and the near equatorial regions. Maximum correlations are close to 1.0 at zero lag, although 0.8 is a more typical value, demonstrating the tight coupling between vortex stretching and meridional transport.

[39] In summary this section has shown evidence that windstress curl variations at the eastern boundary of the subtropical gyre can excite variations in meridional baroclinic transport via their effect on near-surface vertical velocity and subsequently on the vortex stretching term dw/dz, which is tightly coupled to the transport. We have therefore described a three-stage mechanism for the interannual variability: windstress curl induces a response in w_{100m}, this affects dw/dz (vortex stretching) which has to be balanced by meridional transport (and hence changes to the AMOC) due to the conservation of potential vorticity. In the subpolar gyre the link between near surface vertical velocity and vortex stretching is not observed and the interannual variability seems to be forced by a different mechanism. Previous work by *Kanzow et al.* [2010] and *Chidichimo et al.* [2010] have suggested a link between windstress curl at the eastern boundary and excitation of Rossby waves as a
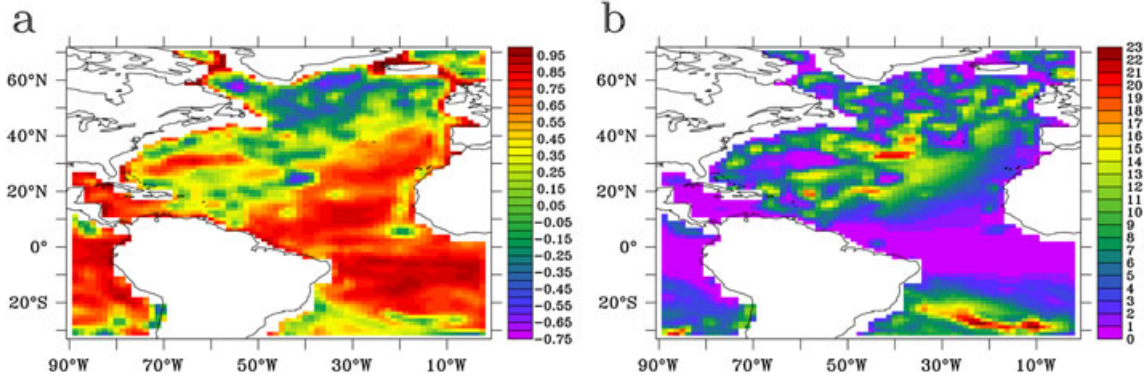
Figure 10. Lagged correlation of dw/dz (i.e., w_{100m}–w_{650m}) against near surface vertical velocity (w_{100m}). (a) Maximum correlation taking account of all lags. (b) Lag in months at which maximum correlation occurs. Vertical velocity has been filtered to retain interannual time scales. The plot is based on monthly mean vertical velocities from years 623–653 of CONTROL (which includes the LOW state of the AMOC), but is typical of the CONTROL and ensemble simulations.

mechanism for AMOC variability, focusing on annual time scales. Here we have shifted the focus to interannual time scales and attempted to explain the physical processes behind the forcing mechanism. Additionally we have tried to estimate to what extent the boundary forcing can explain the sensitivity of the system to initial conditions.

[40] We conclude this section by examining the extent to which the basin-integrated AMOC (rather than local transports) is sensitive to Rossby wave propagation. Figure 12 shows the correlation at various lags, of the AMOC itself with the windstress curl at the eastern boundary. The most obvious feature is a dipole of moderate strength (correlations of order ±0.55) at a lag of about 12 months. The highest correlations are located at ~20°N (positive) and ~50°N (negative). These correlations are lower than those seen for the local transport, but are not negligible. The lag of about 12 months is consistent with the lag between the near surface vertical velocity and subsequent vortex stretching (Figure 10). Thus the basin integrated AMOC owes something to the Rossby wave propagation, but is clearly also influenced by other processes (e.g., western boundary anomalies, discussed in the next and subsequent sections).
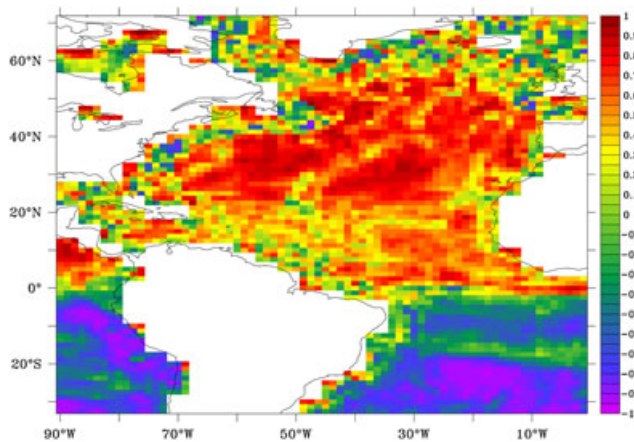
4.6. Example of Wave Propagation Mechanism at 30°N

[41] We provide an example of the wind wave generation mechanism at 30°N to illustrate the above findings and for comparison with extensive observations available in this region. Figures 13a and 13b show a time-latitude diagram of annual mean meridional transport (this time for two members of the HIGH ensemble). In Figure 13a, westward propagation is visible and traceable from the eastern boundary to about 70°W, close to but not coincident with the western boundary. The propagation in velocity is less coherent than that in pressure at this latitude (compare Figures 13c and 13d which show pressure from the same ensemble members) and there appears to be more amplification at the mid-Atlantic ridge. At the western boundary itself, there is more complicated behavior, with larger amplitude, including both westward and eastward propagation, which is not clearly seen in the pressure field and is likely to be advective in origin (section 4.7). The first side panel, Figure 13a, on the right shows the meridional transport (lagged by 6 months) at 20°W (black line) and the corresponding near-surface vertical

Figure 11. Instantaneous correlation of dw/dz (i.e., w_{100m}–w_{650m}) against upper layer baroclinic transport. The plot is based on monthly mean vertical velocities from years 623 to 653 of CONTROL as for Figure 9.
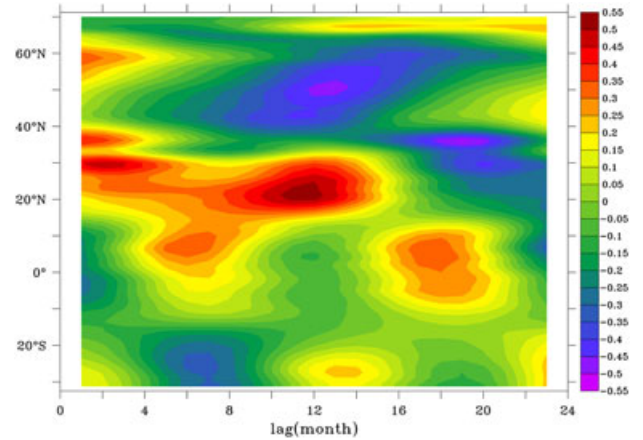

Figure 12. Correlation between windstress curl at the eastern boundary (10°W, 30°N) and the (lagged) AMOC as a function of latitude and lag. The calculation is based on interannually filtered monthly mean data from years 570 to 600 of CONTROL.
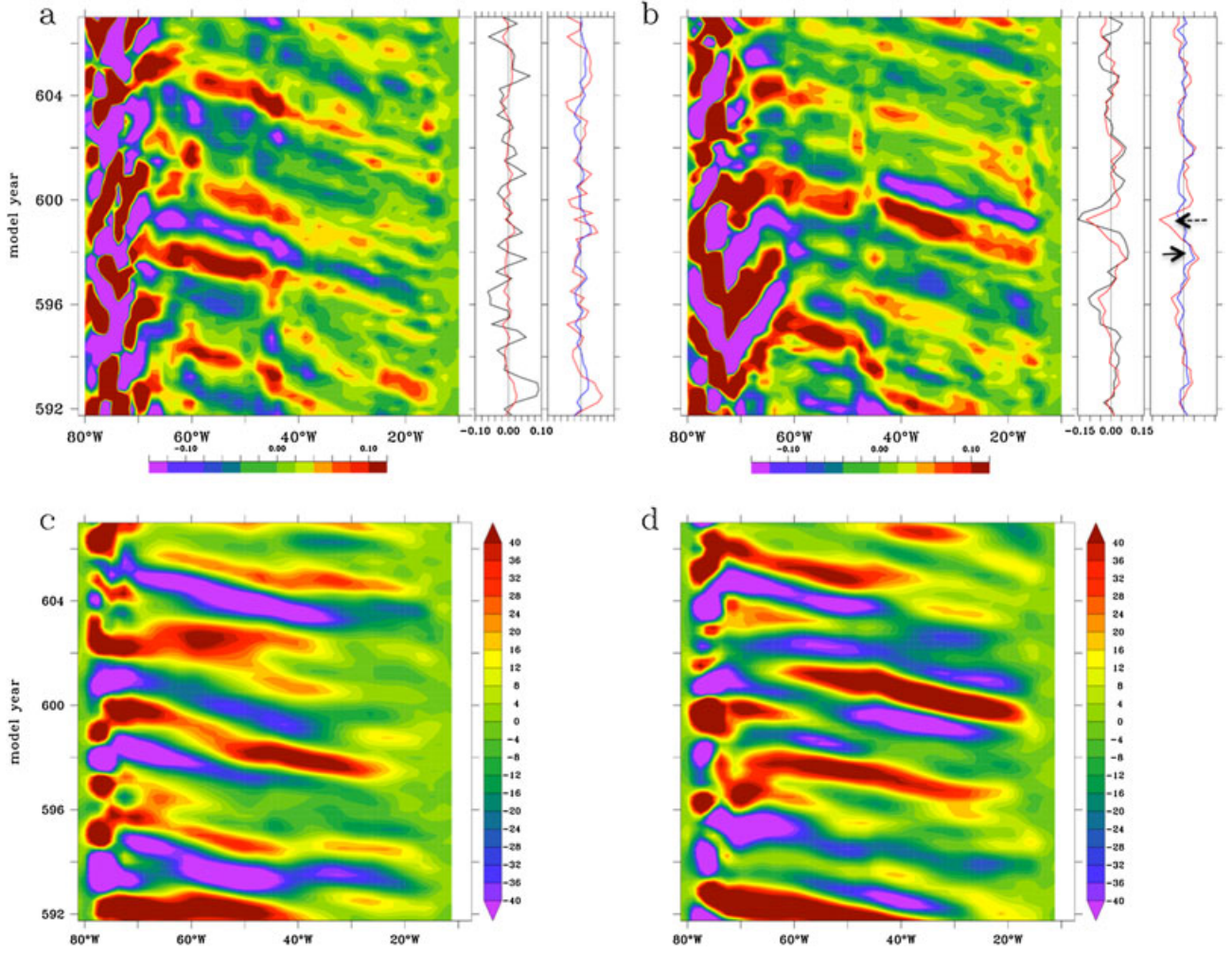
Figure 13. (a) Time-longitude diagram at 30°N of upper layer meridional transport (Sv/gridpoint) for first member of HIGH ensemble. Line plots to the right are values at 20°W of upper layer meridional transport (same units), with a lag of 6 months (black line), near-surface vertical velocity, w_{100m}, (red lines) and windstress curl at the eastern boundary (blue line). We have scaled the vertical velocity and windstress curl on the rightmost line plot by a factor of 2.4 to make them easier to see, and omitted axis labels as these are the same as on the adjacent line plot. (b) similar plot for second member of HIGH ensemble. (c) Time-longitude diagram at 30°N of upper layer baroclinic pressure anomaly (hPa) for first member of HIGH ensemble. (d) Same as Figure 13c for second member of ensemble HIGH. All variables have been filtered to retain interannual time scales.

velocity (red line), w_{100m}, there is a strong correlation as expected from Figure 10 and w_{100m} clearly has an important (but not exclusive) role in forcing the transport fluctuations which subsequently propagate as a wave. The second side panel of Figure 13a, shows the windstress curl at the eastern boundary (blue line) and w_{100m} (red line) and again there is a strong correlation as implied by Figures 8 and 9. The correlation is somewhat weaker however and it is not always possible to attribute fluctuations in w_{100m} to definite changes in windstress curl. Figure 13b shows similar diagrams for another ensemble member and we see here that the large positive fluctuation in transport in year 598 at 20°W is clearly associated both with a fluctuation in w_{100m} and with a positive excursion of the windstress curl (highlighted by the solid arrow). No such excursion in the windstress curl is present at that time in Figure 13a (dashed arrow), supporting the assumption that the difference between the two simulations (including subsequent propagation) is due to differences

in windstress curl. Conversely the strong negative anomaly visible in year 599 (Figure 13b) does not show a very strong negative excursion in the windstress curl, and so this event seems to be influenced by other processes in addition to the windstress curl.

[42] In conclusion, there is a link between windstress curl and transport variations, and this can be used to explain differences which arise between ensemble members, but exact predictions cannot be made as other processes are clearly also present. Nonetheless, a positive (negative) excursion in the windstress curl at the boundary will normally result in a positive (negative) propagating signal in the meridional transport.

4.7. Propagation at the Western Boundary and Summary Diagram

[43] Section 4.6 presented evidence of propagation originating from both eastern and western boundaries (Figure 13). Here we focus on the western boundary propagation in more
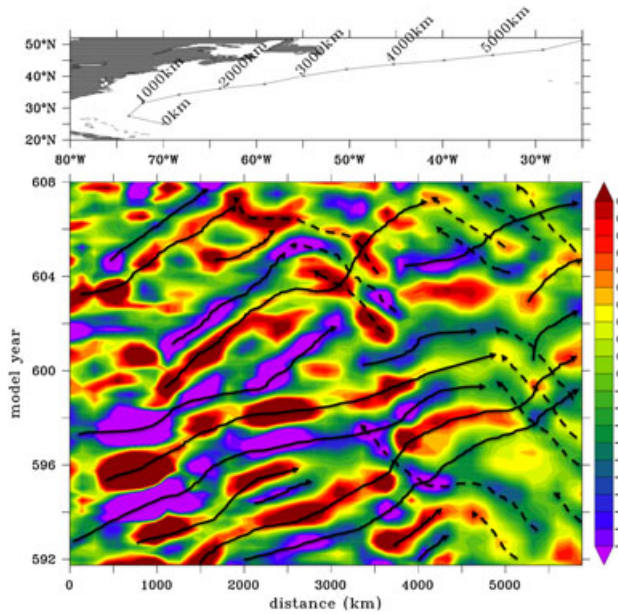
Figure 14. Propagation along the western boundary of the North Atlantic. The upper panel shows a propagation pathway (thin line). The lower panel is a time-distance diagram, showing meridional transport anomalies (Sv) with distance along the western boundary and time. Northeastward and northwestward propagation originate at opposite ends of the Gulf Stream/North Atlantic Current and interact east of the Grand Banks (indicated by arrows). The diagram is based on seasonal mean anomalies from CONTROL, filtered to retain interannual time scales.

detail as well as establishing links between the westward propagating Rossby waves and the eastward propagating anomalies at the western boundary, before summarizing the propagation features found in this study.

[44] Anomaly propagation along the western boundary of the North Atlantic is demonstrated using a time-distance diagram oriented along the path of the Gulf Stream/North Atlantic Current (Figure 14). On interannual time scales, there is clear propagation along the path of the Gulf Stream (solid arrows), i.e., in the wrong direction to be attributed to Rossby or Kelvin-type waves. This poleward propagation seems to be advective in origin as evidenced by the speed of anomaly propagation which is roughly consistent with the speed of the mean currents (c.f. *Sinha et al.* [2004]). The northeastward/eastward propagation can be traced for thousands of kilometres and involves changes to the amplitude and speed of the anomalies en route. There is also evidence of westward propagating anomalies (i.e., going against the Gulf Stream/North Atlantic Current) in the region 25°W–55°W (dashed arrows). These latter are clearly westward (or northwestward) propagating Rossby waves originating from the eastern boundary as previously described. East of the Grand Banks, anomalies being carried eastward interact with westward propagating Rossby waves (and intermittently with anomalies advected southeastward in the Labrador Current), creating a complicated interference pattern (this can be seen in the right hand part of the distance-time diagram in Figure 14 where the horizontal coordinate ranges from 3500–5500 km and the dashed and solid arrows frequently meet and cross over each other).

[45] To provide evidence that the western boundary current anomalies can be linked to the westward moving Rossby waves in the ocean interior, we next plot spatially coherent anomalies at different time periods from one of the members of ensemble HIGH (Figure 15). The sequence begins at year 600 and proceeds in 6 months intervals for 3 years. Here an initially small and weak anomaly at ~25°N, 25°W transforms into a SW-NE oriented wavefront of order 1000 km in length. The wavefront subsequently propagates westwards/northwestwards and intensifies in amplitude. After 2 years, the extreme south-west portion of the wavefront curls clockwise and feed into the western boundary where it subsequently travels eastwards, presumably advected by the Gulf Stream. The westward propagating Rossby waves thus appear to be able to influence transport at the western boundary where meridional transport anomalies are of order ±1 Sv over a model gridcell. An interesting topic for further study would be quantification of the effects of the waves on western boundary current position and strength.

[46] Figure 16 presents a summary of the propagating features detected in the model based on analysis of the upper layer velocities. There is northwestward phase propagation in the subtropical gyre, with coherent wavefronts (e.g., Figure 15) extending for thousands of kilometers from Europe to South America. At the western boundary amplification of anomalies occurs and there is poleward propagation along the coast of North America and along the North Atlantic Current path (Figure 14). A variety of other propagating features were also detected using Hovmöller diagrams and animations (not included in the paper for reasons of conciseness). Anomaly propagation is seen along the Greenland coast extending from Denmark Strait to the Labrador Sea, and this also seems to be advective in origin. In the Equatorial and South Atlantic there is also wave propagation. The oceanic region south of Equatorial West Africa is a source region for southwestward propagating waves, whilst there
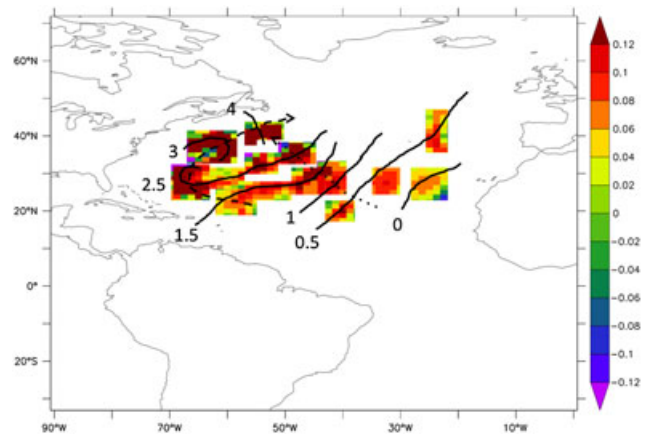
Figure 15. Connection between interior Rossby wave propagation and anomaly propagation at the western boundary. The solid black lines connect spatially coherent anomalies at particular times (relative to year 600) denoted by numerical labels (0, 0.5, 1 year, etc.). Color shading shows meridional transport anomaly from a member of ensemble HIGH. Dotted line and arrow shows the direction of Rossby wave propagation. Dashed line and arrow shows the development and propagation of an anomaly at the western boundary.

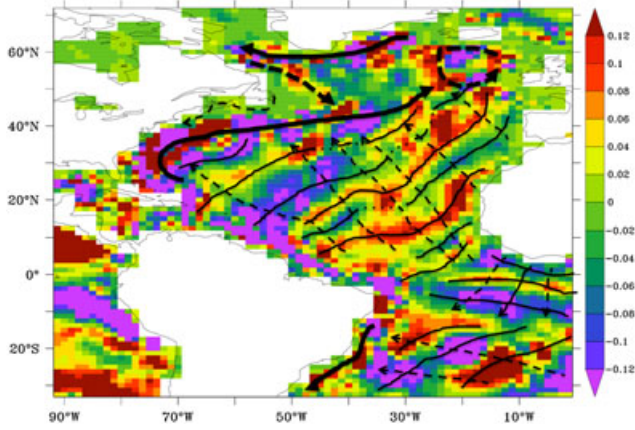**Figure 16.** Summary diagram of wavefronts and propagation directions for the Atlantic. Thin black lines show wavefronts for interannual timescale Rossby wave-like propagating features. Thin dashed arrows show propagation directions for these waves. Thick black lines show boundary propagation, probably advective in origin. Thick dashed arrows show tentative or intermittent propagation, also probably advective in origin. The color shading is the meridional transport anomaly (Sv) for summer of year 633.

are westward propagating waves in the South Atlantic, with, surprisingly, a small northward component to the phase velocity. Southward propagating anomalies on the western boundary of the South Atlantic seem to be advective in origin.

[47] The large northward component of the Rossby waves in the subtropical gyre is interesting and bears further comment. We note that one possible explanation of the apparent northward component is that the westward phase speed of Rossby waves decreases at higher latitudes as β decreases. Waves initiated at the western boundary will reach a given longitude with a delay dependent on latitude which could provide an apparent northward propagation. Set against this is expectation from theory that north-south propagation is permissible [e.g., *Gill*, 1982] and north-south propagation is seen in quasigeostrophic studies with a constant β [*Barnier*, 1988]. The latter author found the direction of phase propagation to be 46° to the northwest, similar to our Figure 15 and emphasized the role of the orientation of the mid-Atlantic Ridge in determining the direction of phase propagation. Animations (not shown) indicate that in HadCM3 the northward component of the propagating waves is somewhat intermittent in time and may also vary spatially.

4.8. Differences in Predictability Between the HIGH and LOW Ensembles

[48] Differences in predictability time for the pressure field at the eastern boundary of the subtropical gyre for the HIGH and LOW ensembles were noted in section 4.4. Figures 17a and 17b show the RMSE normalized by twice the CONTROL standard deviation calculated for the sets of windstress curl for the HIGH and LOW ensembles respectively averaged for lead times up to 2 years. Where this diagnostic is small the windstress curl will have a relatively high predictability (inverse relationship). Ensemble HIGH (Figure 17a) has relatively low predictability time (high RMSE) in the tropical South Atlantic and relatively high predictability time (low RMSE) at around 45°N and in the Gulf Stream region.

Ensemble LOW has relatively low predictability time scale in the eastern subpolar gyre and relatively high predictability time scale south of the Equator and at around 55°W, 20°N. It can be seen that close to the eastern boundary of the subtropical gyre (at 30°N), both HIGH and LOW ensembles have similar, intermediate RMSE values. Windstress at the eastern boundary of the subtropical gyre determines the vertical velocities in the region of the model where westward propagation originates (section 4.5, Figure 8b). Thus the spread in near surface vertical velocity between the ensemble members in the HIGH state would be expected to be similar to the spread between the ensemble members in the LOW state at a given time, and similarly the spread in dw/dz and the baroclinic transport (from the relationships established between these variables in the previous section). Thus the fact that there is little difference in predictability of the transport at 30°N is a consequence of the fact that the windstress at the eastern boundary diverges at the same rate in both ensembles.

[49] In Figures 17a and 17b, at ~45°N we find that there is a relatively long predictability time for the windstress at the
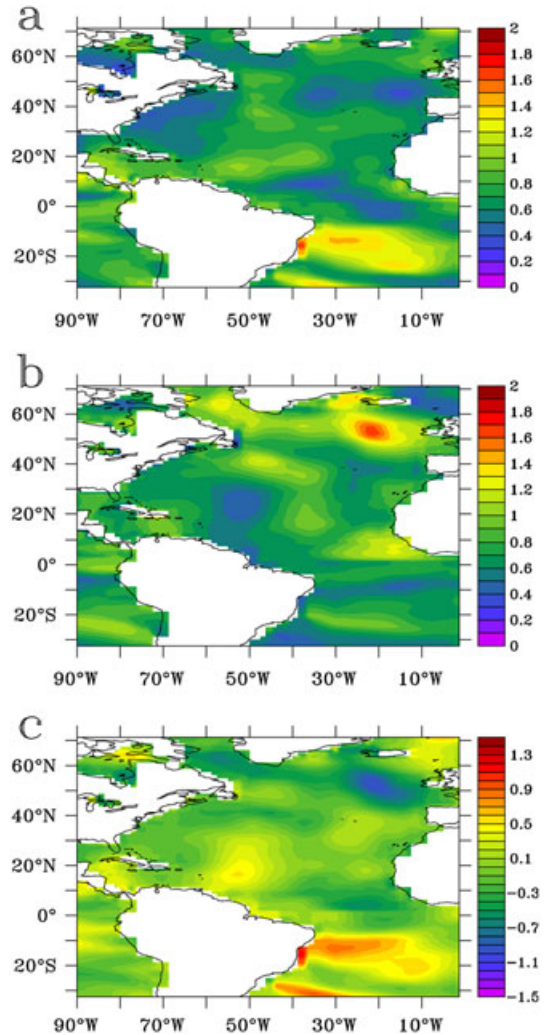

Figure 17. (a) RMSE in ocean surface windstress curl, averaged over lead times up to 2 years for ensemble HIGH, relative to twice the modeled climatological (CONTROL) standard deviation, (b) similar plot for ensemble LOW, and (c) difference in RMSE between HIGH and LOW ensembles.

eastern boundary in the HIGH ensemble (blue area) compared with the LOW ensemble (red area). Figure 8a demonstrates that at 45°N the eastern boundary windstress determines the near-surface vertical velocity field, w_{100m}, in the eastern subpolar gyre. Hence, w_{100m} is more predictable in the eastern subpolar gyre on interannual time scales in the HIGH compared to the LOW ensembles. Whether this impacts on predictability of the subpolar gyre transport remains unclear as we have been unable to establish a link between near-surface vertical velocity and dw/dz (or baroclinic transport) in the subpolar gyre. How the difference in windstress predictability between the ensembles is communicated to differences in transport predictability, if at all, remains unexplained. Nonetheless, Figure 7a (section 4.4) indicates that based on the RMSE measure, the basin integrated AMOC is more predictable in ensemble HIGH compared with LOW.

[50] Differences in RMSE between the two ensembles are shown in Figure 17c highlighting the significant difference in windstress curl predictability between the ensembles at ~55°N (Figure 17c also shows significant differences close to the north coast of South America and in the tropical South Atlantic). The caveat on this result is the small ensemble size and small number of ensembles. Detailed inspection of Figure 17c shows that the RMSE is higher at the eastern boundary (at 30°N) in the LOW ensemble compared to the HIGH ensemble and this is consistent with the slightly longer predictability times found in the HIGH ensemble compared with the LOW ensemble in section 4.4. It is however difficult to directly link (correlate) the RMSE in windstress with the RMSE in w_{100m} (or in dw/dz or the meridional transport). This is because RMSE is a nonlinear measure, and although there is a strong correlation between curl τ at the eastern boundary and w_{100m}, and also between the difference in these quantities between individual pairs of ensemble members (Figures 8 and 9), the process of calculating RMSE leads to amplification of the residual error in the correlations.

5. Summary

[51] We have elucidated a mechanism leading to loss of predictability of the ocean circulation on interannual time scales in a coupled climate model with a noneddying ocean component. Even in a noneddying ocean, and away from the surface Ekman layer (i.e., below about 100 m depth), small differences in initial atmospheric conditions cause changes in the Rossby wave field which dominates pressure and transport variability on interannual time scales in the interior ocean. The pressure changes translate to changes in the baroclinic transport via the geostrophic relation which holds to a reasonable degree throughout the domain. Changes appear first close to the eastern boundary and propagate westwards, resulting in longer predictability time in the interior of the western basin compared to the east. North-south baroclinic transport in the interior ocean is strongly linked to vortex stretching (i.e., dw/dz) and in the subtropical gyre region close to the eastern boundary the latter is controlled to a large extent by eastern boundary wind stress curl through its influence on near surface vertical velocity, resulting in a regime where variability is dominated by Rossby wave propagation. This contrasts with the subpolar gyre where the eastern boundary windstress curl does not have a strong

influence on vortex stretching and interannual variability is not strongly dominated by Rossby wave activity.

[52] The western boundary is also a region of relatively rapid loss of predictability, and we have shown that this area is dominated by propagation of transport anomalies along the Gulf Stream path, probably by advection by mean currents. The source of these anomalies is not fully clear, but we have demonstrated that Rossby wavefronts reaching the western boundary can initiate anomalies which amplify and subsequently propagate along the Gulf Stream. Apart from local effects in the interior ocean, eastern boundary windstress curl and Rossby wave propagation clearly affect the basin integrated transport variability. Precise quantification is however difficult and requires further study.

[53] We also explored the dependence of the transport predictability on interannual timescales on the mean state of the AMOC (high versus low). At both 30°N and 45°N there is evidence of slightly longer predictability times in ensemble HIGH close to the eastern boundary. At 30°N the eastern boundary windstress curl is slightly more predictable in HIGH than in LOW which is consistent with the small difference in predictability time scale. However, further north, at 45°N, there is significantly longer predictability of windstress curl when the AMOC is in a strong (high) state and this may result in slightly longer predictability times for the transport compared to when the AMOC is in a weak (low) state.

6. Discussion and Conclusions

[54] We conclude that on interannual time scales westward propagating baroclinic Rossby waves generated by fluctuations in windstress curl have an important effect on the variability and predictability of North Atlantic meridional transports in the HadCM3 climate model. There is a clear indication that the basin integrated AMOC is also affected (in particular anomalies due to Rossby wave propagation are of the same order of magnitude as fluctuations in the basin wide AMOC), but other processes are also involved, for example generation and propagation of transport anomalies at the western boundary. Western boundary anomalies interact with eastward propagating Rossby waves, but the implications for western boundary current position and variability are still unclear. The good agreement between simulated and observed meridional transport and its variability at 26°N gives some confidence that similar mechanisms could be operating in the real world.

[55] Whilst of intrinsic interest in terms of ocean variability, the implications of our study for predictability of regional heat/salt transports and surface fluxes of heat and freshwater need to be explored. It is not at present clear whether the propagation of Rossby waves on these time scales has a significant effect on weather or climate variability, and this can only be ascertained by investigating whether the atmosphere feels any influence from these oceanic processes. Potentially, heat flux convergence due to propagating waves could affect the atmospheric boundary layer—such effects have mainly been demonstrated in the more energetic western boundary current regions [e.g., *Minobe et al.*, 2008].

[56] The presence of mesoscale ocean eddies will modify our results to an unknown extent, hence studies of

predictability in climate models using eddy-permitting (or even eddy-resolving) ocean components [*Delworth et al.*, 2012] will need to be conducted.

[57] Feedbacks to/from the atmosphere have not been addressed by our study, which has concentrated on the reasons for initial divergence of model trajectories. It remains unclear how and why the windstress predictability differs in certain regions depending on the state of the AMOC and even whether this is a robust result. A more comprehensive study with many more ensembles would have to be conducted to test this rigorously.

[58] Our study may be model dependent, therefore similar mechanistic studies should be conducted on other climate models (e.g., the CMIP5 initial condition ensemble experiments [*Taylor et al.*, 2012]). Propagation speeds and directions as well as regions of susceptibility to perturbations may well be different in different models (e.g., depending on the grid type, the resolution or the time step). Nevertheless, Rossby/boundary wave propagation are well established mechanisms that have been simulated in a wide range of ocean models [e.g., *Barnier*, 1988; *Lecointre et al.*, 2008; *Aoki et al.*, 2009; *Hunt et al.*, 2012]. Previous studies have also shown that Rossby and boundary waves are likely to be linked to fluctuations of meridonal ocean transports [e.g., *Hirschi et al.*, 2007; *Roussenov et al.*, 2008] providing further support to the existence of a possible link between baroclinic waves and the predictability of ocean transports.

References

Aoki, K., A. Kubokawa, H. Sasaki, and Y. Sasai (2009), Midlatitude baroclinic Rossby waves in a high-resolution OGCM simulation, *J. Phys. Oceanogr.*, *39*, 2264–2279, doi:10.1175/2009JPO4137.1.

Balan Sarojini, B., J. M. Gregory, R. Tailleux, G. R. Bigg, A. T. Blaker, D. R. Cameron, N. R. Edwards, A. P. Megann, L. C. Shaffrey, and B. Sinha (2011), High frequency variability of the Atlantic meridional overturning circulation, *Ocean Sci.*, *7*, 471–486, doi:10.5194/os-7-471-2011.

Barnier, B. (1988), A numerical study on the influence of the Mid-Atlantic Ridge on nonlinear 1st-mode baroclinic Rossby waves generated by seasonal winds, *J. Phys. Oceanogr.*, *18*(3), 417–433, doi:10.1175/1520-0485(1988)018<0417:ANSOTI>2.0.CO;2.

Chelton, D. B., M. G. Schlax, R. M. Samelson, and R. A. De Szoeke (2007), Global observations of large oceanic eddies, *Geophys. Res. Lett.*, *34*(15), L15606, doi:10.1029/2007GL030812.

Chidichimo, M. P., T. Kanzow, S. A. Cunningham, W. E. Johns, and J. Marotzke (2010), The contribution of eastern-boundary density variations to the Atlantic meridional overturning circulation at 26.5 N, *Ocean Sci.*, *6*, 475–490, doi:10.5194/os-6-475-2010.

Cipollini, P., D. Cromwell, G. Quartly, and P. G. Challenor (1999), Remote Sensing of oceanic extra-tropical Rossby waves, in *Satellites, Oceanography and Society, Elsevier Oceanogr. Ser.*, vol. 63, edited by D. Halpern, pp. 99–123, Elsevier Sciences, Amsterdam.

Collins M. (2002), Climate predictability on interannual to decadal time scales: the initial value problem, *Clim. Dyn.*, *19*, 671–692, doi:10.1007/s00382-002-0254-8.

Collins, M., and B. Sinha (2003), Predictability of decadal variations in the thermohaline circulation and climate, *Geophys. Res. Lett.*, *30*(6), doi:10.1029/2002GL016504.

Cunningham, S. A., et al. (2007), Temporal variability of the Atlantic meridional overturning circulation at 26.5°N, *Science*, *317*, 935–938.

Delworth, T. L., S. Manabe, and R. J. Stouffer (1993), Interdecadal variations of the thermohaline circulation in a coupled ocean-atmosphere model, *J. Climate*, *6*, 1993–2011.

Delworth, T. L., et al. (2012), Simulated climate and climate change in the GFDL CM2.5 High-resolution coupled climate model, *J. Clim.*, *25*, 2755–2781, doi:10.1175/JCLI-D-11-00316.1.

Dong, B., and R. T. Sutton (2002), Variability in North Atlantic heat content and heat transport in a coupled ocean-atmosphere GCM, *Clim. Dyn.*, *18*, 485–497.

Dong, B., and R. T. Sutton (2005), Mechanism of interdecadal thermohaline circulation variability in a coupled ocean-atmosphere GCM, *J Clim.*, *19*, 1117–1135.

Gerdes, R., and C. Wübber (1991), Seasonal variability of the North-Atlantic Ocean – a model intercomparison, *J. Phys. Oceanogr.*, *21*(9), 1300–1322, doi:10.1175/1520-0485(1991)021<1300:SVOTNA>2.0.CO;2.

Gill, A. E. (1982), *Atmosphere-Ocean Dynamics, Int. Geophys. Ser.*, vol. 30, Academic Press, London.

Gordon, C., C. Cooper, C. A. Senior, H. T. Banks, J. M. Gregory, T. C. Johns, J. F. B. Mitchell, and R. A. Wood (2000), The simulation of SST, sea ice extents and ocean heat transports in a version of the Hadley Centre coupled model without flux adjustments, *Clim. Dyn.*, *16*, 147–168.

Gregory, J. M., and R. Tailleux (2011), Kinetic energy analysis of the response of the Atlantic meridional overturning circulation to CO_2-forced climate change, *Clim. Dyn.*, *37*, 893–914, doi:10.1007/s00382-010-0847-6.

Griffies, S. M., and K. Bryan (1997), A predictability study of simulated North Atlantic multidecadal variability, *Clim. Dyn.*, *13*, 459–487.

Hawkins, E., and R. T. Sutton (2007),Variability of the Atlantic thermohaline circulation described by three-dimensional empirical orthogonal functions. *Clim. Dyn.*, *29*, 745–762.

Hirschi, J. J.-M., P. D. Killworth, and J. R. Blundell (2007), Subannual, seasonal and interannual variability in the North Atlantic meridional overturning circulation, *J. Phys. Oceanogr.*, *37*, 1246–1265, doi:10.1175/JPO3049.1.

Hirschi, J. J.-M., P. D. Killworth, and J. R. Blundell (2009), Sea surface height signals as indicators for oceanic meridional mass transports, *J. Phys. Oceanogr.*, *39*, 581–601.

Hirschi, J. J.-M., A. T. Blaker, B. Sinha, A. Coward, B. de Cuevas, S. Alderson, and G. Madec (2012), Chaotic variability of the meridional overturning circulation on subannual to interannual timescales, *Ocean Sci. Discuss.*, *9*, 3191–3238, doi:10.5194/osd-9-3191-2012.

Hunt, F. K., R. Tailleux, and J. J.-M. Hirschi (2012), The vertical structure of oceanic Rossby waves: a comparison of high-resolution model data to theoretical vertical structure, *Ocean Sci.*, *8*, 19–35, doi:10.5194/os-8-19-2012.

Kanzow, T., H. L. Johnson, D. P. Marshall, S. A. Cunningham, J. J.-M. Hirschi, A. Mujahid, H. L. Bryden, and W. E. Johns (2009), Basinwide integrated volume transports in an eddy-filled ocean, *J. Phys. Oceanogr.*, *39*(12), 3091–3110, doi:10.1175/2009JPO4185.1.

Kanzow, T., et al. (2010), Seasonal variability of the Atlantic meridional overturning circulation at 26.5°N, *J. Climate*, *23*, 5678–5698, doi:10.1175/2010JCLI3389.1.

Killworth, P. D., and J. R. Blundell (2003), Long Extratropical Planetary Wave Propagation in the Presence of Slowly Varying Mean Flow and Bottom Topography. Part II: Ray Propagation and Comparison with Observations, *J. Phys. Oceanogr.*, *33*, 802–821.

Killworth, P. D., and J. R. Blundell (2007), Planetary wave response to surface forcing and instability in the presence of mean flow and topography, *J. Phys. Oceanogr.*, *37*, 1297–1320, doi:10.1175/JPO3055.1.

Lecointre, A., T. Penduff, P. Cipollini, R. Tailleux, and B. Barnier (2008), Depth dependence of westward-propagating North Atlantic features diagnosed from altimetry and a numerical 1/6 degrees model, *Ocean Science*, *4*(1), 99–113, doi:10.5194/os-4-99-2008.

Lippert, A., and R. H. Kase (1985), Stochastic wind forcing of baroclinic Rossby waves in the presence of a meridional boundary, *J. Phys. Oceanogr.*, *15*(2), 184–194, doi:10.1175/1520-0485(1985)015<0184:SWFOBR>2.0.CO;2.

Manabe, S., and R. J. Stouffer (1988), Two Stable Equilibria of a Coupled Ocean-Atmosphere Model, *J. Clim.*, *1*, 841–866.

Mason, E., F. Colas, J. Molemaker, A. F. Schepetkin, C. Troupin, J. C. McWilliams, and P. Sangra (2011), Seasonal variability of the Canary Current: a numerical study, *J. Geophys. Res.*, *116*, C06001, doi:10.1029/2010JC006665.

Minobe, S., A. Kuwano-Yoshida, K. Nobumasa, S.-P. Xie, and R. J. Small (2008), Influence of the Gulf Stream on the troposphere, *Nature*, *452*, 206–210, doi:10.1038/nature06690.

Polito, P. S., and P. Cornillon (1997), Long baroclinic Rossby waves detected by TOPEX/POSEIDON, *J. Geophys. Res.*, *102*(C2), 3215–3235, doi:10.1029/96JC03349.

Pingree, R., and B. Sinha (2001), Westward moving waves or eddies (Storms) on the Subtropical/Azores Front near 32.5°N? Interpretation of the Eulerian currents and temperature records at moorings 155 (35.5°W) and 156 (34.4°W), *J. Mar. Syst.*, *29*(1–4), 239–276.

Roussenov, V. M., R. G. Williams, C. W. Hughes, and R. J. Bingham (2008), Boundary wave communication of bottom pressure and overturning changes for the North Atlantic, *J. Geophys. Res.*, *113*, C08042, doi:10.1029/2007JC004501.

Siedler, A., and M. Finke (1993), Long-period transport changes in the eastern North-Atlantic and their simulation by propagating waves, *J. Geophys. Res.*, *98*, 2393–2406, doi:10.1029/92JC02122.

Sime, L. C., D. P. Stevens, K. J. Heywood, and K. I. C. Oliver (2006), A decomposition of the Atlantic meridional overturning, *J. Clim.*, *36*, 2253–2270.

Sinha, B., B. Topliss, and J. Harle (2004), Eastward propagating surface anomalies at ocean gyre boundaries, *J. Geophys. Res.*, *109*, C12005, doi:10.1029/2004JC002392.

Smith, D. M., S. Cusack, A. W. Colman, C. K. Folland, G. R. Harris, and J. M. Murphy (2007), Improved surface temperature prediction for the coming decade from a global climate model, *Science*, *317*, 796–799, doi:10.1126/science.1139540.

Sturges, W., and B. G. Hong (1995), Wind forcing of the Atlantic thermocline along 32°N at low frequencies, *J. Phys. Oceanogr.*, *25*(7), 1706–1715, doi:10.1175/1520-0485(1995)025<1706:WFOTAT>2.0.CO;2.

Taylor, K. E., R. J. Stouffer, and G. A. Meehl (2012), An overview of CMIP5 and the experiment design," *Bull. Am. Meteor. Soc.*, *93*, 485–498, doi:10.1175/BAMS-D-11-00094.1.

Vellinga, M., and P. Wu (2004), Low-latitude freshwater influence on centennial variability of the Atlantic thermohaline circulation, *J. Clim.*, *17*, 4498–4511.